Sustainable Development Research; Vol. 7, No. 2; 2025
ISSN 2690-9898 E-ISSN 2690-9901
https://doi.org/10.30560/sdr.v7n2p85

Research on the Construction of $CuFeS_2$/ Bi_2O_3 Composite Materials and Degradation of Bisphenol A by Activating PMS

Shiqi Huang[1] & Jingjing Xu[1]

[1] Jiangsu Key Laboratory of Atmospheric Environment Monitoring and Pollution Control, School of Environmental Science and Engineering, Collaborative Innovation Center of Atmospheric Environment and Equipment Technology, Jiangsu Engineering Technology Research Center of Environmental Cleaning Materials, Nanjing University of Information Science and Technology, Nanjing, China

Correspondence: Jingjing Xu, Jiangsu Key Laboratory of Atmospheric Environment Monitoring and Pollution Control, School of Environmental Science and Engineering, Collaborative Innovation Center of Atmospheric Environment and Equipment Technology, Jiangsu Engineering Technology Research Center of Environmental Cleaning Materials, Nanjing University of Information Science and Technology, Nanjing 210044, China.

Received: April 17, 2025 Accepted: May 21, 2025 Online Published: May 23, 2025

Abstract

Bisphenol A (BPA) is harmful to human health. Advanced oxidation technologies using peroxymonosulfate (PMS) can effectively remove organic pollutants. Among these technologies, bimetallic sulfides stand out for their excellent activation ability. This study focuses on $CuFeS_2$, and $CuFeS_2$/Bi_2O_3 catalysts were prepared using a hydrothermal method. The CFSBO-2/PMS system can degrade up to 84.06% of BPA in just 30 seconds. XRD analysis shows that compared to the original CFS, the CFSBO catalyst significantly enhances the intensity of diffraction peaks, indicating improved crystallinity. The system maintains high degradation efficiency as the pH increases from 3.6 to 9.0, suggesting that the catalyst is highly adaptable to different water treatment conditions. The main active species generated are SO_4−•, •OH, and $^1O_2$. PMS activation in this system is driven by the redox cycles of Cu^+/Cu^{2+}, Fe^{2+}/Fe^{3+}, and Bi^{3+}/Bi^{5+}.

Keywords: PMS Activation Technology, $CuFeS_2$/Bi_2O_3, Bisphenol A

1. Introduction

Bisphenol A (BPA) poses a potential risk to human health. Advanced oxidation techniques that use peroxymonosulfate (PMS) are particularly effective at breaking down organic pollutants. Bimetallic sulfides, in contrast to single-metal sulfides, offer greater surface area, quicker electron transfer, and enhanced catalytic efficiency. Bi_2O_3 stands out for its environmental compatibility and cost-effectiveness, with its unique electronic structure promoting the transfer of electrons on the catalyst surface. In a study by Jing and colleagues [1], a Z-type heterojunction Bi_2O_3@$NiFe_2O_4$ material was synthesized. This material was used to activate PMS in a photodegradation process, effectively breaking down the antibiotic ofloxacin (OFX) in wastewater. This suggests that Bi_2O_3 could be an effective catalyst for PMS activation, even in the absence of light. Li and colleagues [2] successfully synthesized a $CuFe_2O_4$/Bi_2O_3 catalyst using a simple sol-gel method based on citric acid complexes. This catalyst was designed to break down TC-HCl in organic wastewater. In the absence of light, the degradation rate of TC-HCl activated by PMS increased from 56.2% to 95.7% within 60 minutes, and the catalyst worked effectively across a wide pH range (3-11).

This study successfully prepared the $CuFeS_2$/Bi_2O_3 composite material and applied it to activate PMS for the removal of BPA. The material was characterized using various analytical techniques, and its performance as a catalyst for activating PMS to break down BPA was assessed. The effects of catalyst dosage, PMS concentration, initial pH, and inorganic anions on BPA degradation were systematically investigated. The study also explored the potential of this technology for pollution control. Bi_2O_3 is expected to reduce the aggregation of CuFeS2, helping to enhance the redox cycling of transition metals.

2. Materials and Methods

2.1 Preparation of $CuFeS_2$/Bi_2O_3 Composite Materials

Bi_2O_3 is a chemical reagent purchased for the laboratory, referred to as BO. The $CuFeS_2$/Bi_2O_3 composite material is prepared using a hydrothermal method. To begin, equal amounts (0.01 mol) of copper(I) chloride and ferric

chloride hexahydrate are added to 55 mL of ultrapure water. Next, 10 mL of 14% ammonium sulfide solution is gradually added to this mixture. After stirring for 30 minutes, varying amounts of Bi_2O_3 are introduced into the solution, followed by another 30 minutes of stirring. The solution is then placed in a 100 mL Teflon-lined stainless steel autoclave. Then that is heated to 200°C for 10 hours. After, the product is filtered and washed with ultrapure water, then dried at 60°C for 12 hours. The resulting powder is ground into a fine powder, and the samples are named $CuFeS_2/Bi_2O_3$ (abbreviated as CFSBO). Based on the molar ratio of $CuFeS_2$ to Bi_2O_3 (9:1, 10:1, and 11:1), the corresponding samples are labeled CFSBO-1, CFSBO-2, and CFSBO-3. The pure $CuFeS_2$ is made without adding BO and is called CFS.

2.2 Characterization of the Catalyst

The crystalline architecture and phase composition of the photocatalytic material were analyzed using X-ray diffraction (XRD, XRD-6100, Shimadzu, Japan). The scanning speed was 7°/min, with a 2θ range from 10° to 80°. The surface chemistry and bonding were examined using X-ray photoelectron spectroscopy (XPS, Thermo Kalpha, Thermo Fisher, USA). The catalyst's morphology was observed using transmission electron microscopy (TEM, JEM F200, Japan).

2.3 Experimental Procedures and Testing Methods

In this study, unless stated otherwise, all experiments were conducted in a 100 mL beaker under light-exclusion conditions, with stirring provided by a magnetic stirrer. The degradation experiments were carried out in this setup. Typically, the catalyst (0.4 g/L) was added to a 100 mL solution of BPA (5 mg/L). Then stirred for 40 minutes at a temperature of 25 ± 2°C (in the dark) in order to reach an adsorption-desorption equilibrium. After this, PMS (0.12 mM) was added to start the reaction. The time when the equilibrium was achieved, before the PMS was added, was considered the 0-second mark. Once PMS was added, timing began immediately. Samples were periodically extracted at 0, 10, 30, 60, and 180 s time points. To quench the reaction, 1 mL of methanol was added to the sample, followed by 3 mL of the reaction mixture. The mixture was then centrifuged and through a 0.45 μm PTFE filter membrane. The collected samples were analyzed by HPLC (70% chromatographic-grade methanol and 30% ultra-pure water). The concentration of BPA was determined using HPLC with a C18 column (150 mm × 4.6 cm, 3.5 μm). In experiments assessing the effects of anions and quenching agents, both were added simultaneously. The reaction was continued for 40 minutes in the dark. To evaluate the stability of the catalyst, it was subjected to three washing cycles with anhydrous ethanol and ultrapure water after each reaction. Followed by centrifugation and drying for recovery. The catalyst was then collected and used in cyclic experiments following this procedure.

3. Results and Discussion

3.1 Catalyst Characterization

From Figure 1, we can see that the 2θ peaks of CFS, which were prepared using the hydrothermal method, appear at 29.39°, 49.08°, and 57.89°, corresponding to the CFS (112), (204), and (312) crystal planes, respectively [3, 4]. When comparing the XRD of the purchased BO with the standard card (JCPDS NO:71-2274), the peaks at 26.904°, 27.392°, 33.256°, and 46.334° correspond to the (111), (120), (200), and (221) planes. In the CFSBO composite material, the relative content of each phase changes due to different amounts of BO in CFSBO-1 compared to CFSBO-2 and CFSBO-3. The composite samples show clear characteristic peaks of BO at 27.392° and 46.334° and a peak for CFS at 29.39°. Moreover, the intensity of the diffraction peaks increases significantly after combining BO and CFS, indicating that the composite has improved crystallinity and confirming that the composite material was successfully prepared.

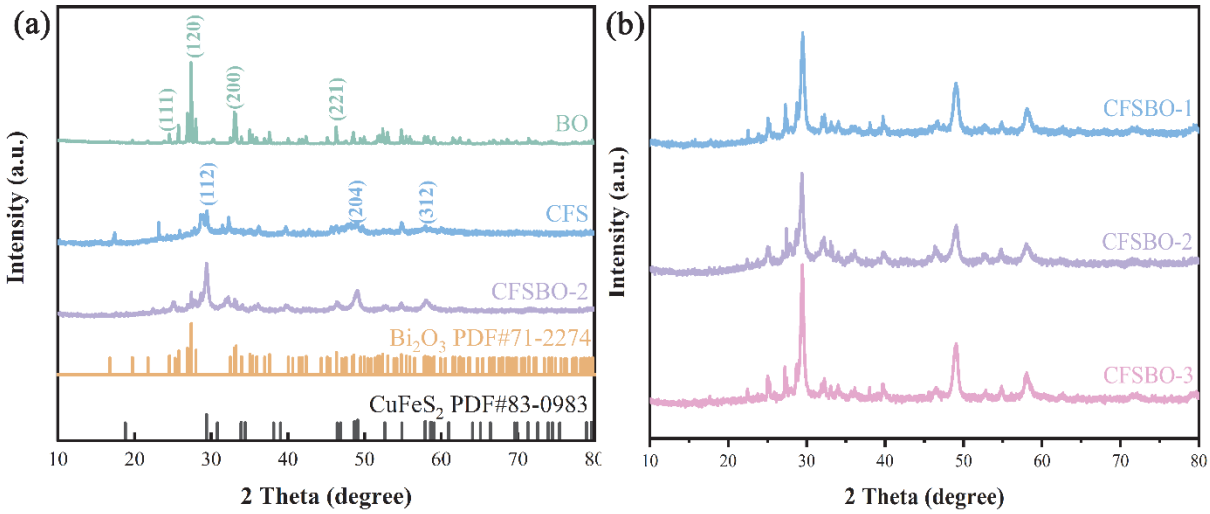

Figure 1. XRD patterns of BO, CFS and CFSBO composite samples

The surface morphology and microstructure of the pure CFS, BO, and CFSBO-2 samples were examined using TEM and HRTEM. As shown in Figure 2a, the CFS sample appears amorphous. In Figure2b, the pure BO shows a mixture of rod-like and block-like structures. Figure 2c displays the TEM image of CFSBO-2, where both CFS and rod-like BO can be seen, indicating a close interface between the two materials. In the HRTEM image in Figure 2d, lattice fringes corresponding to the crystal structures of both CFS and BO are visible. The 0.31 nm spacing matches the (012) plane of BO, while the 0.187 nm spacing matches the (220) plane of CFS, further confirming the successful preparation of the composite material.

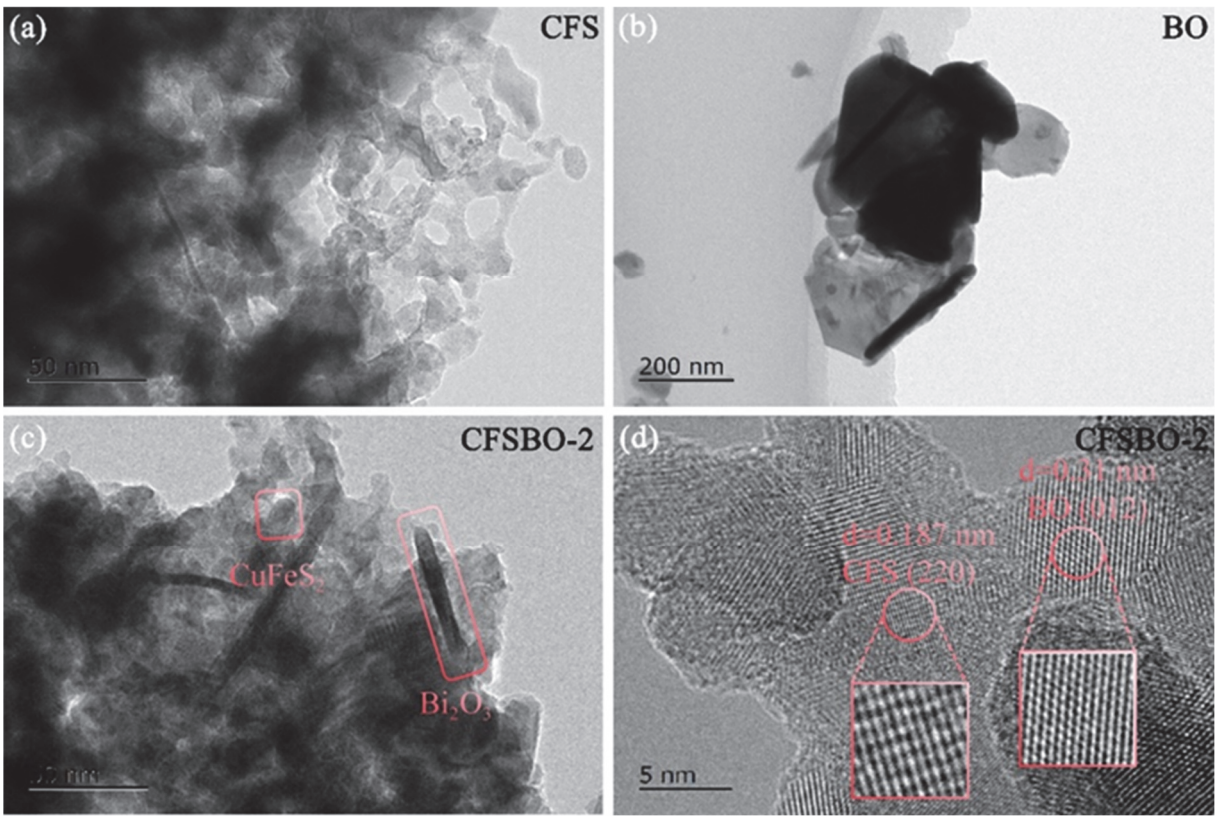

Figure 2. (a) TEM images of CFS. (b) TEM images of BO. (c) TEM images of CFSBO-2. (d) HRTEM images of CFSBO-2

As shown in Figure 3a, all elements of the catalyst are present in the full spectrum. The XPS spectra of Cu 2p, Fe 2p, S 2p, Bi 4f, and O 1s of the catalyst are shown in Figures 3b-e. From Figure 3a, it can be observed that Cu, Fe, S, Bi, and O elements are present in the prepared CFS/BO composite catalyst, indicating successful synthesis of the composite catalyst. From Figure 3b, the peaks of Cu $2p_{3/2}$ and Cu $2p_{1/2}$ in the pure CFS sample appear at binding energies of 932.13 eV and 952.02 eV, which indicate that Cu is primarily present in the +1 oxidation state in CFS [5]. Cu^{2+} is mainly present as $Cu(OH)_2$ on the surface of CFS, with binding energies of 932.69 eV and 956.05 eV [6]. In the composite sample CFSBO-2, the binding energies of Cu $2p_{3/2}$ and Cu $2p_{1/2}$ are 932.31 eV and 952.19 eV. It is observed that the binding energy of Cu 2p in the composite sample shifts towards higher binding energies, which may be due to the change in electron cloud density after the composite, potentially aiding in the activation of PMS to produce more reactive oxygen species [7]. Figure 3c shows the high-resolution O 1s spectra. In the pure BO sample, the peaks at 529.96 eV and 531.09 eV are attributed to the O 1s orbitals, and the same peaks are observed in the composite sample CFSBO. The peak at 532.41 eV is attributed to surface-adsorbed -OH or H_2O [8]. After composite formation, the binding energies of O 1s shift to higher binding energies, which might be due to changes in the electron cloud density after the composite. However, it is notable that in CFSBO-2, the peak at 530.18 eV significantly weakens, and the peak at 531.93 eV noticeably strengthens. This may be due to the transformation of lattice oxygen (O_2^-) into oxygen vacancies after the composite, which is usually accompanied by a reduction in the oxidation state of active redox cations. This is confirmed by the enhancement of the peak at 708.03 eV in the Fe 2p spectrum [9, 10]. From Figure 3d, it can be seen that in both the pure CFS and CFSBO composite samples, the peaks at 708.9 eV and 708.03 eV correspond to the Fe^{2+} peak in Fe $2p_{3/2,}$ which may be attributed to Fe^{2+}-S [11]. In the pure CFS sample, the peak at 711.40 eV corresponds to Fe^{2+} in Fe $2p_{3/2}$, the peak at 713.64 eV corresponds to Fe^{3+} in Fe $2p_{3/2}$, the peak at 723.17 eV corresponds to Fe^{2+} in Fe $2p_{1/2}$, and the peak at 725.60 eV corresponds to Fe^{3+} in Fe $2p_{1/2}$, which is consistent with literature reports [12-15]. In the CFSBO composite sample, the peaks for Fe^{2+} in Fe $2p_{3/2}$, Fe^{3+} in Fe $2p_{1/2}$, and Fe^{2+} in Fe $2p_{1/2}$ shift towards higher binding energies to 714.57 eV, 724.94 eV, and 728.65 eV, respectively, indicating that the electronic cloud density has changed after composite formation. Notably, the peak at 724.94 eV becomes stronger, while the peak at 728.65 eV becomes weaker, which may promote the Fe^{3+}/Fe^{2+} cycling efficiency, thereby enhancing pollutant degradation [16]. Figure 3e shows the high-resolution spectra for S 2p and Bi 4f. In the pure BO sample, the peak at 159.19 eV corresponds to Bi $4f_{7/2}$, and the peak at 164.51 eV corresponds to Bi $4f_{5/2}$, indicating that Bi exists in the +3 oxidation state in the pure sample. In the CFSBO composite sample, the two peaks of Bi 4f shift to higher binding energies, indicating that the electron cloud density of Bi has increased and that the surface electronic structure has changed. Moreover, a peak at 158.50 eV appears in the composite sample, corresponding to Bi^{3+} $4f_{7/2}$, suggesting that Bi has transitioned to a lower oxidation state [8, 17, 18]. In Figure 3e, the four main peaks of S 2p are located at 161.36 eV, 162.25 eV, 163.26 eV, and 164.62 eV, corresponding to S_2^-, S_2^{2-}, S_n^{2-}, and S_0, respectively. In addition, peaks at 168.84 eV and 170.05 eV indicate that SO_4^{2-} has been oxidized by air [19]. However, in the CFSBO composite sample, the binding energies of the corresponding peaks shift slightly towards higher binding energies.

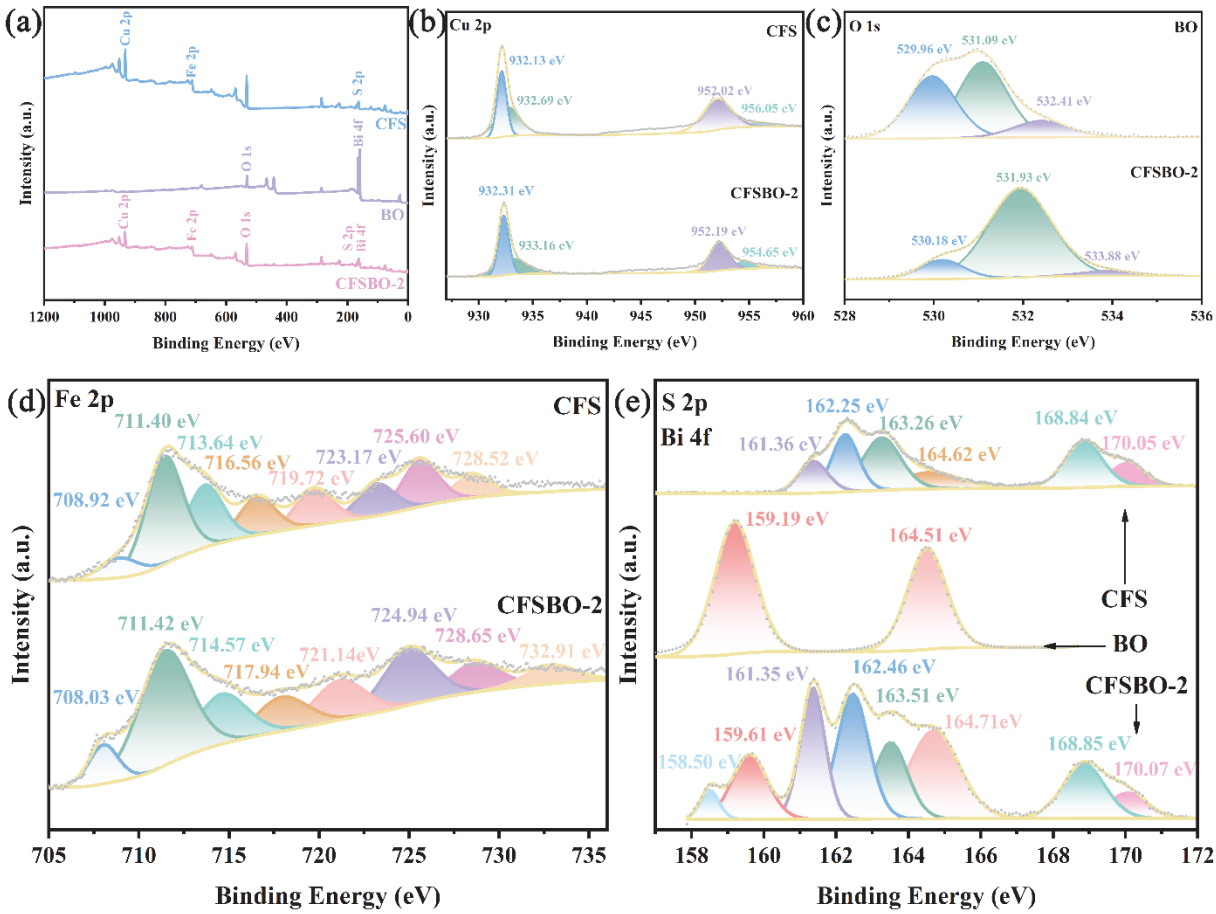

Figure 3. High-resolution XPS spectra of CFS, BO and CFSBO-2: (a) Full-spectrum (b) Cu 2p (c) O 1s (d) Fe 2p (e) S 2p, Bi 4f

3.2 Research on Degradation

This study conducted a series of experiments under light-shielded conditions to evaluate the catalyst's ability. As shown in Figure 4a, the initial experiment tested the degradation of BPA by CFS, BO, CFSBO-1, CFSBO-2, and CFSBO-3 without PMS. It was observed that these materials had very little effect on BPA degradation, with their highest degradation efficiencies being only 1.95%, 1.47%, 1.43%, 2.24%, and 2.11%, respectively. Additionally, HPLC testing revealed that CFSBO-1, CFSBO-2, and CFSBO-3 only had a minimal adsorption effect on BPA. The next step examined the degradation of BPA using PMS, CFS/PMS, BO/PMS, CFSBO-1/PMS, CFSBO-2/PMS, and CFSBO-3/PMS. In the absence of a catalyst, PMS alone was able to degrade BPA to a maximum of 2.41%, which is in line with what has been reported in the literature [20]. BO showed almost no ability to activate PMS for BPA degradation, with a maximum efficiency of only 2.36%. However, when CFS, CFSBO-1, CFSBO-2, and CFSBO-3 were used to activate PMS, the degradation efficiency of BPA significantly increased, reaching 35.10%, 77.03%, 86.08%, and 77.77%, respectively. The improvements were particularly noticeable, with CFSBO-1, CFSBO-2, and CFSBO-3 achieving degradation efficiencies 2.19, 2.45, and 2.22 times greater than that of pure CFS. Additionally, the degradation efficiency of CFSBO-2 was 36.47 times higher than BO. While the degradation efficiencies of CFSBO-1, CFSBO-2, and CFSBO-3 showed slight variations, they all successfully activated PMS to degrade BPA. This demonstrates that combining CFS and BO enhances the ability under the same concentrations of pollutant (5 ppm) and PMS (0.12 mM). Therefore, it is concluded that CFS and BO, when combined, improve the activation performance of CFS. Based on the highest degradation efficiencies observed with CFSBO-1, CFSBO-2, and CFSBO-3, CFSBO-2 was selected for further experimentation, including the investigation of factors influencing the catalyst's ability to activate PMS for BPA degradation and the reusability of CFSBO-2.

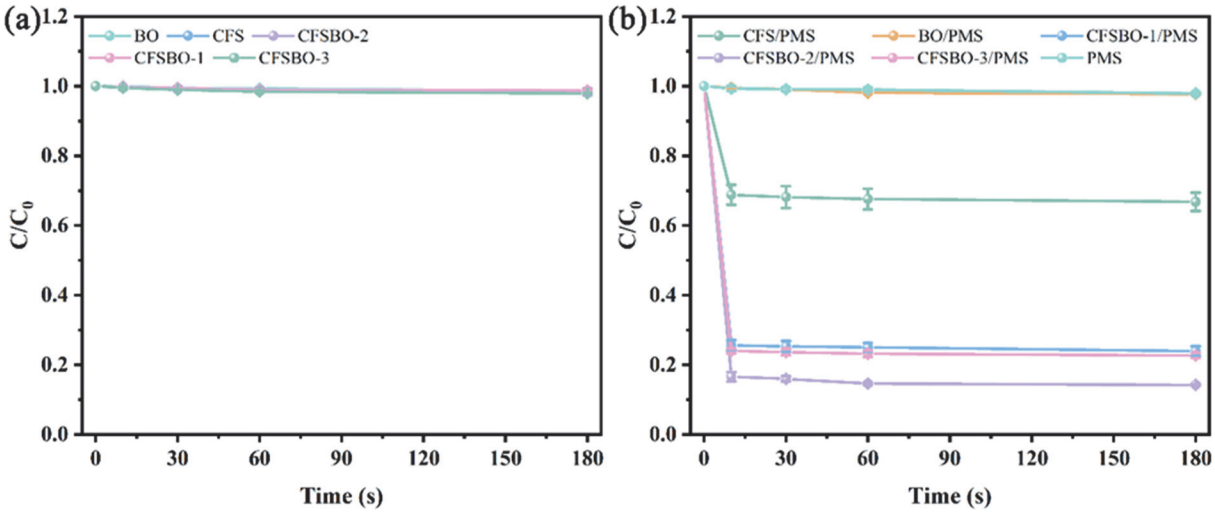

Figure 4. (a) Degradation curves of BPA under different conditions of catalyst dosage. (b) Degradation curves of BPA under different PMS concentration conditions

3.3 Factors Effect on Degradation

This study further examined the impact of the amount of CFSBO-2 on PMS activation for BPA degradation, using a consistent PMS concentration of 0.12 mM. It was clear that the catalyst amount had little effect on the PMS activation efficiency in degrading BPA. To determine the optimal catalyst dosage, 30 mg, 40 mg, and 50 mg of CFSBO-2 were added to 100 mL of the pollutant system, and the BPA degradation efficiency was measured. As shown in Figure 5a, the degradation results were almost identical for 30 mg and 40 mg of the catalyst, with efficiencies of 83.63% and 84.20%, respectively. When 30 mg of CFSBO-2 was used, the degradation efficiency was slightly lower compared to 40 mg, likely because 30 mg produced fewer reactive species to activate PMS. This suggests that, within a certain range, increasing the catalyst amount can provide more active sites, enhancing the degradation efficiency [21]. However, when the amount of CFSBO-2 was increased to 50 mg, the degradation efficiency dropped by 9.23%. This could be due to an excess of catalyst negatively affecting BPA degradation [22]. This shows that increasing the catalyst amount can improve degradation efficiency by providing more surface area and active sites to activate PMS, but beyond an optimal amount, the excess catalyst can reduce efficiency [23]. Based on these findings and considering the cost-effectiveness, 40 mg of CFSBO-2 was selected as the optimal catalyst amount for future experiments.

With 40 mg of CFSBO-2 added, the study then explored how different concentrations of PMS affected BPA degradation. As detailed in the previous chapter, the PMS concentration was varied (0.03 mM, 0.06 mM, 0.09 mM, 0.12 mM, and 0.15 mM) to observe the degradation of BPA. The results, shown in Figure 5b, revealed that when 40 mg of CFSBO-2 activated lower concentrations of PMS (0.03 mM, 0.06 mM, and 0.09 mM), the degradation efficiencies were limited, at 14.83%, 38.34%, and 64.65%, respectively. The increase in degradation efficiency was primarily due to a higher production of free radicals over time, which accelerated BPA degradation. However, when PMS concentrations were increased to 0.12 mM and 0.15 mM, the degradation rate did not continue to rise proportionally, and only at 0.15 mM was there a slight improvement in degradation within the first 10 seconds. This suggests that at these concentrations, PMS activation reaches a saturation point, and further increases in PMS concentration do not significantly enhance degradation efficiency. It is likely that the limited catalyst was unable to activate the excess PMS. Based on these results and considering economic factors, 4 mg was deemed the optimal PMS concentration for the following experiments.

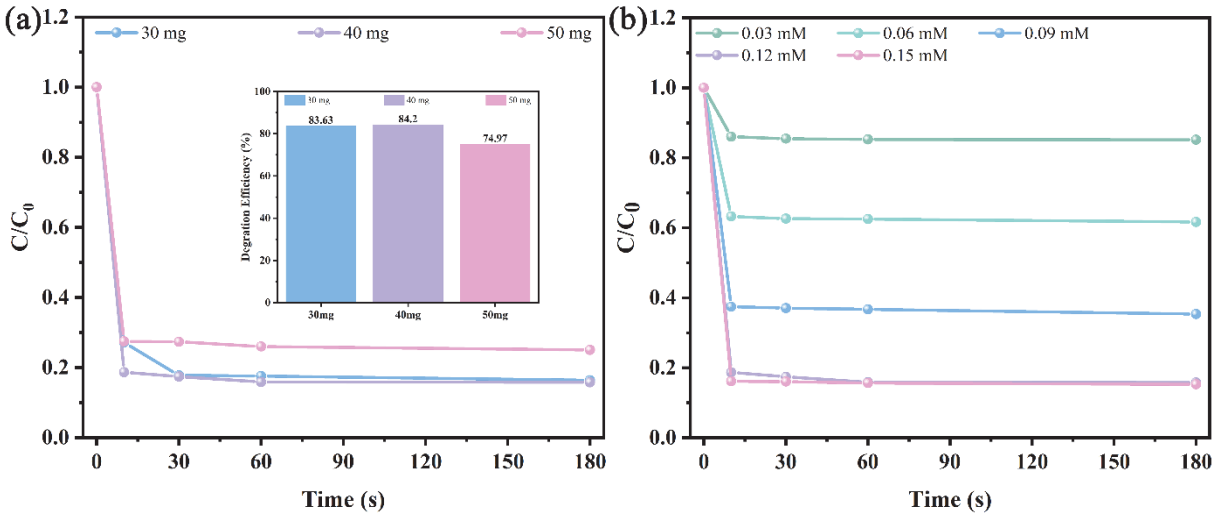

Figure 5. (a) Degradation curves of BPA under different conditions of catalyst dosage. (b) Degradation curves of BPA under different PMS concentration conditions

Since pH can affect the charge properties and surface structure of the catalyst, its impact on the degradation of BPA in the CFSBO-2/PMS system was studied across a pH range of 3.6 to 9.0, as shown in Figure 6a. In the control experiment with an initial pH of 3.6, the degradation efficiency reached 84.20%. The reaction in the control experiment was nearly complete within 10 seconds. As the pH increased, the efficiency of the CFSBO-2 catalyst in activating PMS to degrade BPA within 10 seconds significantly decreased, and a longer time was needed to activate PMS for BPA degradation. When the initial pH was adjusted to 5.0 and 7.0, the degradation efficiencies were 81.88% and 81.67%, respectively, showing little decrease. This might be due to the self-buffering effect of the CFSBO-2 catalyst, which helps stabilize the pH of the solution [24]. However, at a pH of 9.0, the CFSBO-2 catalyst showed slight inhibition of BPA degradation, with a 19.33% drop in efficiency. This could be because, under alkaline conditions, SO_4^{-}• radicals can be converted into •OH radicals [24-26], which is not as effective for degrading BPA. The •OH radicals have a much shorter lifespan (<1 μs) compared to SO_4^{-}• (which lasts 10-30 μs). Moreover, PMS can undergo hydrolysis in alkaline conditions, reducing the amount of PMS available and thus inhibiting the generation of reactive oxygen species (ROS) [27]. Additionally, at pH 9.0, the reduction in H^+ concentration promotes the generation of SO_5^{2-}, which accelerates the self-decomposition of PMS into $^1O_2$. However, this process lowers the efficiency of PMS and reduces the chance of active species interacting with BPA, leading to a decrease in BPA removal. Furthermore, OH^- ions can also inhibit PMS activation [28].

Inorganic anions are commonly found in actual wastewater, so it's crucial to understand how they affect the activation of PMS in degrading BPA. In this study, NaCl, NaH_2PO_4, Na_2SO_4, $NaCO_3$, and Na_2HPO_4 were used to provide Cl^-, $H_2PO_4^-$, SO_4^{2-}, HCO_3^-, and HPO_4^{2-}, respectively. The results of how these inorganic anions impact BPA removal are shown in Figure 6b. The findings indicate that, compared to the blank experiment, adding Cl^- and SO_4^{2-} slightly enhanced the BPA degradation, with Cl^- boosting the degradation efficiency by 9.40%. Adding SO_4^{2-} improved the efficiency by 4.43%. As explained in the previous section, this could be because Cl^- reacts with SO_4^{-}• to form less active chlorine free radicals (Cl• or $ClOH^-$•). Though less active, these chlorine radicals still have some oxidation power and might continue to break down BPA. [29-31]. The addition of SO_4^{2-} didn't have much impact on BPA degradation. This is because SO_4^{2-} reacts with •OH to form SO_4^{-}•, which is more stable and lasts longer but is produced in smaller amounts, limiting its effect. As a result, there was little change in overall degradation efficiency. When HCO_3^- was added, it had the strongest inhibitory effect on BPA degradation. HCO_3^- is a well-known scavenger of reactive species like SO_4^{-}•, •OH, and $^1O_2$ [32]. After adding $H_2PO_4^-$, the degradation efficiency dropped significantly to 23.66%. This decline may be because $H_2PO_4^-$ acts as a chelating agent, blocking PMS molecules from attaching to and converting at active sites. It might also react with •OH and SO_4^{-}• to form less active new radicals, which slows down BPA degradation. The degradation efficiency dropped even further to 13.44% after adding HPO_4^{2-}, likely due to HPO_4^{2-} reacting with •OH and SO_4^{-}• to create new radicals with even less activity, further hindering BPA degradation [33]. This study provides valuable insights for optimizing advanced oxidation processes (AOPs), especially when dealing with wastewater containing specific anions, suggesting that strategies should be adjusted accordingly.

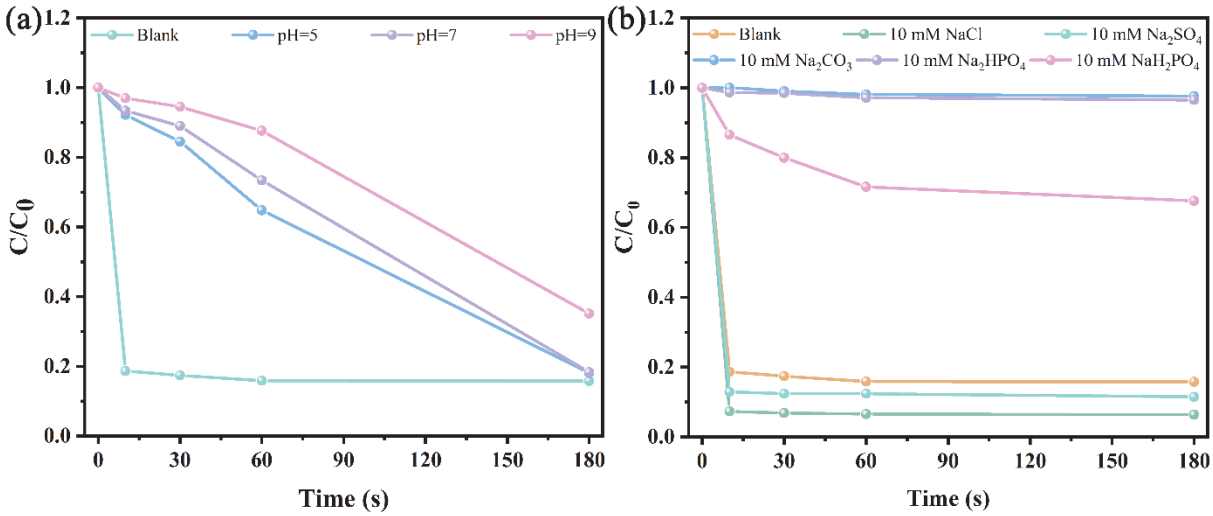

Figure 6. (a) Degradation curves of BPA at different initial pH values. (b) Influence curve of inorganic anions on the degradation of BPA

3.4 Research on the Stability of CFSBO

The stability of the catalytic system is essential for its practical use. To examine the cycling stability of CFSBO-2 nanoparticles as a heterogeneous catalyst, the used catalyst was separated by centrifugation, then washed with anhydrous ethanol and ultrapure water, and dried before being used in the next cycle of experiments. A series of five consecutive degradation tests were carried out to activate PMS with CFSBO-2. As shown in Figure 7, the catalyst's performance dropped from 86.08% in the first cycle to 54.41% in the fifth. The degradation efficiency of the second cycle was 83.39%, slightly lower than the first cycle by 2.78%. In the third cycle, the performance decreased significantly to just 58.13%. Further investigation after the third cycle revealed that the catalyst's performance continued to decline. Based on the results from these cyclic tests, the catalyst was analyzed using XRD after five cycles. As shown in Figure 8, the peaks remained consistent with those before the reaction, and no additional peaks appeared, indicating that the crystal structure had not undergone significant changes.

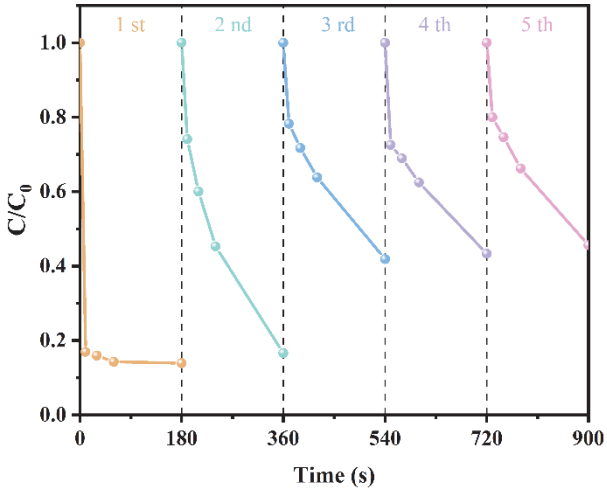

Figure 7. Cyclic degradation of BPA by CFSBO-2/PMS system.

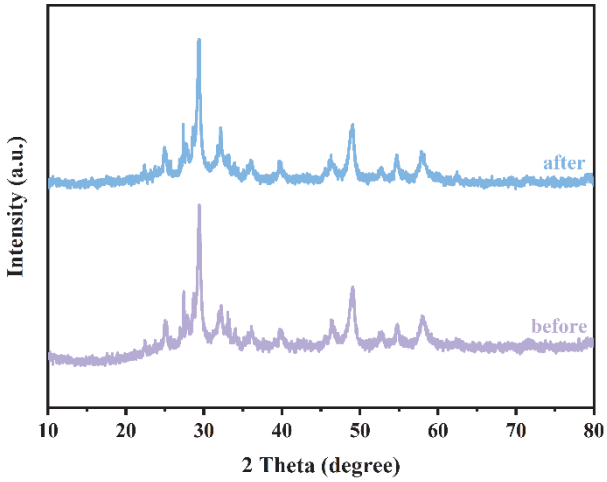

Figure 8. XRD of CFSBO-2 samples before and after cycling

3.5 Reaction Mechanism

To identify which reactive oxygen species (ROS) are primarily involved in the degradation of BPA in the CFSBO-2/PMS system, radical scavenger experiments were conducted. Previous studies have identified SO_4^{-}•, •OH, $^1O_2$, and O_2^{-}• as the main ROS in PMS systems [34, 35]. Methanol (MeOH) was used to scavenge •OH and SO_4^{-}•, while tert-butyl alcohol (TBA) was used specifically for •OH. Quinone (BQ) and histidine (L-His) were introduced to quench O_2^{-}• and $^1O_2$ [36]. As shown in Figure 9, when MeOH was added to the reaction, BPA degradation dropped significantly from 86.08% to 16.20%, highlighting the role of SO_4^{-}• and •OH in removing BPA. However, adding TBA resulted in only a slight decrease, reducing it to 70.92%, a decrease of just 15.16%. This suggests that •OH's contribution to BPA degradation is limited, while SO_4^{-}• plays a more dominant role. Introducing L-His and BQ into the system also led to reduced BPA degradation, with efficiencies dropping to 67.65% and 76.67%, respectively. This indicates that both O_2^{-}• and $^1O_2$ also contribute to BPA removal. From these results, we can conclude that in the CFSBO-2/PMS system, BPA degradation mainly follows a pathway dominated by SO_4^{-}•, with •OH, O_2^{-}•, and $^1O_2$ playing supportive roles in a cooperative free radical mechanism.

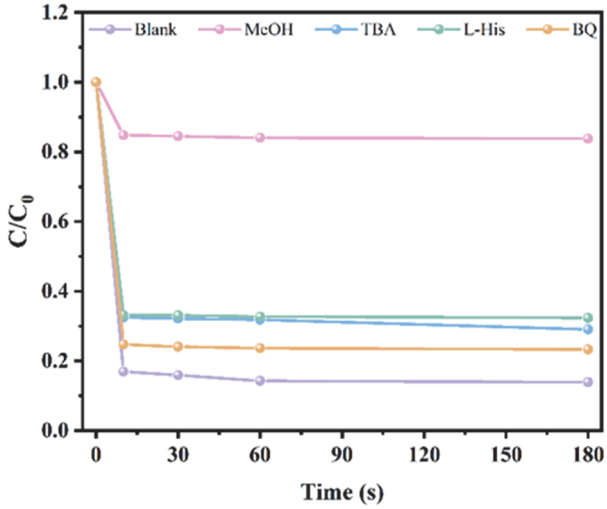

Figure 9. Quenching experiment of active species during the degradation of BPA by CFSBO-2 catalyst

Based on the results of the quenching experiments and XPS analysis, a potential mechanism diagram has been proposed. The activation of PMS appears to involve a key process of valence state cycling within the system, specifically the transitions between Cu^{+}/Cu^{2+}, Fe^{2+}/Fe^{3+}, and Bi^{3+}/Bi^{5+} [37, 38]. The detailed degradation mechanism is illustrated in Figure 10. In CFSBO-2, $Fe^{2+}/Cu^{+}/Bi^{3+}$ ions quickly adsorb onto the surface of CFSBO-

2 and activate PMS, resulting in the generation of sulfate radicals (SO_4^{-}•) and hydroxyl radicals (•OH), as shown in Equations (1) and (2). The catalyst regenerates by reacting with PMS, where high-valence metal ions are reduced to their low-valence counterparts. Specifically, $Fe^{3+}/Cu^{2+}/Bi^{5+}$ are reduced to $Fe^{2+}/Cu^{+}/Bi^{3+}$ while also generating •OH, as outlined in Equation (3) [39]. On the surface of $CuFeS_2$, the Cu^{2+} and Fe^{3+} ions are reduced back to Cu^{+} and Fe^{2+} by strong reducing sulfur species like S^{2-} and S22−, as described in Equations (4-7). According to literature, the standard electrode potentials for these reactions are: $E_{Cu^{2+}/Cu^{+}}$= 0.17 V, $E_{Fe^{3+}/Fe^{2+}}$= 0.77 V and $E_{Bi^{5+}/Bi^{3+}}$= 1.59 V enabling the regeneration of Fe/Cu and Bi/Cu cycles, as shown in Equations (8) and (9) [2]. The generation of •OH can also occur through the reaction of SO4−• with water, as shown in Equation (10). Additionally, 1O2 might form through the weak oxidation of SO5−• with water, as depicted in Equations (11) and (12), or through the interaction of O2−• with •OH, as seen in Equations (13-15). Ultimately, BPA is degraded through the action of SO4−•, •OH, and 1O2, as outlined in Equation (16).

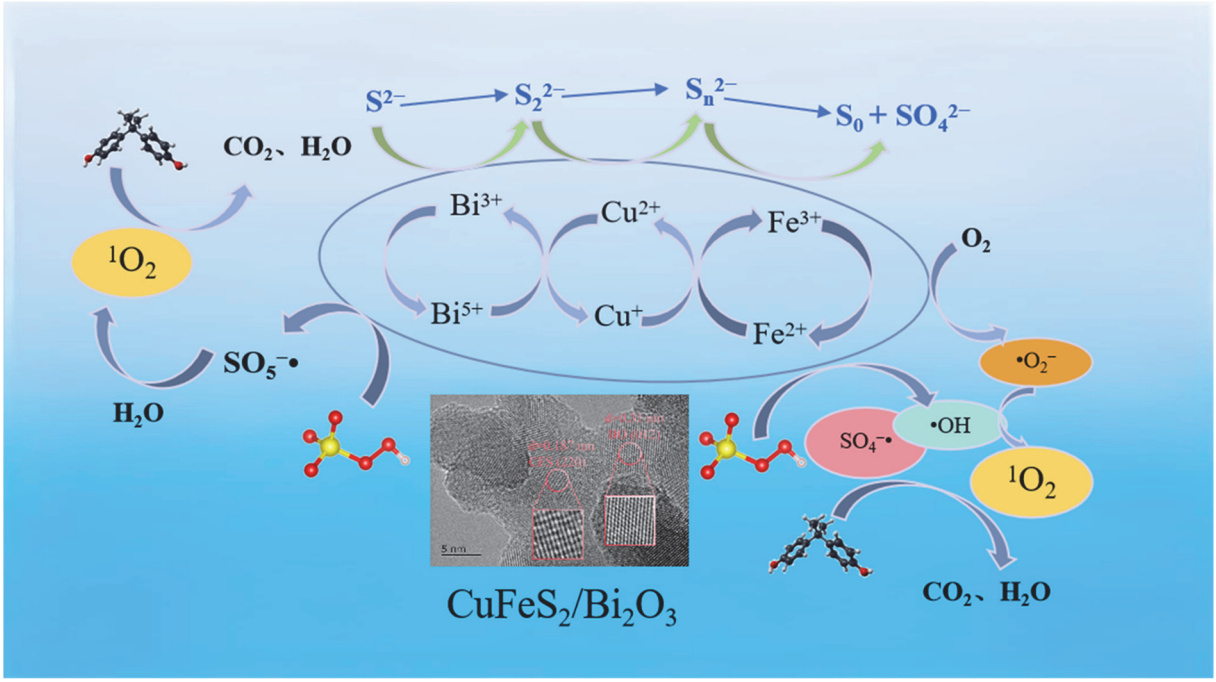

Figure 10. Mechanism diagram of CFSBO-2 activating PMS to degrade BPA.

$$Fe^{2+}/Cu^{+}/Bi^{3+}+HSO_5^{-}\rightarrow Fe^{3+}/Cu^{2+}/Bi^{5+}+SO_4^{-}\bullet+OH^{-} \quad (1)$$

$$Fe^{2+}/Cu^{+}/Bi^{3+}+HSO_5^{-}\rightarrow Fe^{3+}/Cu^{2+}/Bi^{5+}+SO_4^{2-}+\bullet OH \quad (2)$$

$$Fe^{3+}/Cu^{2+}/Bi^{5+}+HSO_5^{-}\rightarrow Fe^{2+}/Cu^{+}/Bi^{3+}+SO_4^{2-}+\bullet OH \quad (3)$$

$$Fe^{3+}/Cu^{2+}/Bi^{5+}+S^{2-}\rightarrow Fe^{2+}/Cu^{+}/Bi^{3+}+S_2^{2-} \quad (4)$$

$$Fe^{3+}/Cu^{2+}/Bi^{5+}+S_2^{2-}\rightarrow Fe^{2+}/Cu^{+}/Bi^{3+}+S_n^{2-} \quad (5)$$

$$Fe^{3+}/Cu^{2+}/Bi^{5+}+S_n^{2-}\rightarrow Fe^{2+}/Cu^{+}/Bi^{3+}+S_0 \quad (6)$$

$$Fe^{3+}/Cu^{2+}/Bi^{5+}+S_0\rightarrow Fe^{2+}/Cu^{+}/Bi^{3+}+SO_4^{2-} \quad (7)$$

$$Fe^{3+}+Cu^{+}\rightarrow Fe^{2+}+Cu^{2+} \quad (8)$$

$$Bi^{5+}+Cu^{+}\rightarrow Bi^{3+}+Cu^{2+} \quad (9)$$

$$SO_4^{-}\bullet+H_2O\rightarrow SO_4^{2-}+\bullet OH+H^{+} \quad (10)$$

$$Fe^{3+}/Cu^{2+}/Bi^{5+}+HSO_5^{-}\rightarrow Fe^{2+}/Cu^{+}/Bi^{3+}+SO_5^{2-}+H^{+} \quad (11)$$

$$2SO_5^{-}\bullet+H_2O\rightarrow 2HSO_4^{-}+1.5^1O_2 \quad (12)$$

$$O_2+e^{-}\rightarrow O_2^{-}\bullet \quad (13)$$

$$2O_2^-\bullet + \bullet OH \rightarrow {}^1O_2 + H_2O_2 \quad (14)$$

$$2O_2^-\bullet + \bullet OH \rightarrow {}^1O_2 + OH^- \quad (15)$$

$$SO_4^-\bullet + \bullet OH + {}^1O_2 + BPA \rightarrow \text{degraded production} \quad (16)$$

5. Conclusion

In this study, CFSBO nanoparticles were successfully prepared using a simple one-step hydrothermal method. Thanks to the straightforward preparation process and readily available materials, this method can be used for removing BPA from contaminated water in emergency situations. The research examined how factors such as the amount of catalyst and PMS added, initial pH levels, and the presence of different anions affected the efficiency of pollutant removal. X-ray diffraction (XRD) analysis showed that the composite had a high crystallinity after synthesis. The best catalytic performance was observed when the molar ratio of CFS to BO was 10:1. In the CFSBO-2/PMS system, under optimal conditions (catalyst concentration of 40 mg, PMS concentration of 4 mg, and the original pH), BPA degradation reached 86.08% within 30 seconds at a concentration of 5 mg/L. The CFSBO-2 material showed good adaptability across a wide pH range (3.0 to 9.0), making it highly suitable for treating various water bodies. Free radical scavenging experiments indicated that PMS was activated through redox cycles involving Cu^+/Cu^{2+}, Fe^{2+}/Fe^{3+}, and Bi^{3+}/Bi^{5+}. The main radicals involved in the BPA degradation process were $SO_4^-\bullet$, $\bullet OH$, and $^1O_2$.

Acknowledgments

This work was supported by the National Natural Science Foundation of China (51978342) and Jiangsu Planned Projects for Postdoctoral Research Funds (No. 2021K414C).

References

[1] Jing, L., Quan, R., Kong, X., & et al. (2025). Enhanced and synergistic catalytic peroxymonosulfate activation degradation of OFX by photoexcitation driven Bi2O3@NiFe2O4 Z−scheme heterojunction. *Colloids and Surfaces A: Physicochemical and Engineering Aspects, 31*, 136773. https://doi.org/10.1016/j.colsurfa.2025.136773

[2] Li, Y., Zhu, C., Chen, L., & et al. (2023). Self-driven degradation of TC-HCl by CuFe2O4/Bi2O3 activated peroxymonosulfate. *Chemical Engineering Journal, 473*, 145282. https://doi.org/10.1016/j.cej.2023.145282

[3] Girma, W. M., Tzing, S.-H., Tseng, P.-J., & et al. (2018). Synthesis of cisplatin(IV) prodrug-tethered CuFeS2 nanoparticles in tumor-targeted chemotherapy and photothermal therapy. *ACS Applied Materials & Interfaces, 10*(5), 4590–4602. https://doi.org/10.1021/acsami.7b16108

[4] Fan, T.-E., Tang, X., Liu, S.-M. (2022). CuFeS2 nanosheets assembled into honeycomb-like microspheres as stable high-capacity anodes for sodium-ion batteries. *ACS Applied Nano Materials, 5*(8), 10392–10398. https://doi.org/10.1021/acsanm.2c01745

[5] Fang, L., Zhang, D., Chen, H., & et al. (2024). Efficient removal of moxifloxacin through PMS activation by CuFeS2/MXene. *Environmental Science and Pollution Research, 31*(32), 45353–45369. https://doi.org/10.1007/s11356-024-34123-9

[6] Wang, H., Liao, B., Hu, M., & et al. (2022). Heterogeneous activation of peroxymonosulfate by natural chalcopyrite for efficient remediation of groundwater polluted by aged landfill leachate. *Applied Catalysis B: Environmental, 300*, 120744. https://doi.org/10.1016/j.apcatb.2021.120744

[7] Jia, Y., Yang, K., Zhang, Z., & et al. (2023). Heterogeneous activation of peroxymonosulfate by magnetic hybrid CuFe2O4@N-rGO for excellent sulfamethoxazole degradation: Interaction of CuFe2O4 with N-rGO and synergistic catalytic mechanism. *Chemosphere, 313*, 137392. https://doi.org/10.1016/j.chemosphere.2022.137392

[8] Li, H., Yang, C., He, Y., & et al. (2023). Oxygen vacancies facilitated photocatalytic detoxification of three typical contaminants over graphene oxide surface embellished BiOCl photocatalysts. *Advanced Powder Technology, 34*(3), 103971. https://doi.org/10.1016/j.apt.2023.103971

[9] De Souza, R. A., & Mueller, D. N. (2021). Electrochemical methods for determining ionic charge in solids. *Nature Materials, 20*(4), 443–446. https://doi.org/10.1038/s41563-021-00947-7

[10] Walsh, A., Sokol, A. A., Buckeridge, J., & et al. (2018). Oxidation states and ionicity. *Nature Materials, 17*(11), 958–964. https://doi.org/10.1038/s41563-018-0165-7

[11] Cheng, D., Yuan, S., Liao, P., & et al. (2016). Oxidizing impact induced by mackinawite (FeS) nanoparticles

at oxic conditions due to production of hydroxyl radicals. *Environmental Science & Technology, 50*(21), 11646–11653. https://doi.org/10.1021/acs.est.6b03492

[12] Ren, X., An, J., Ding, S., & et al. (2025). High efficiency degradation of RhB by MIL-88A(Fe)/MoS2 activated persulfate and its mechanism. *Journal of Solid State Chemistry, 341*, 125027. https://doi.org/10.1016/j.jssc.2025.125027

[13] Liu, N., Huang, W., Zhang, X., & et al. (2018). Ultrathin graphene oxide encapsulated in uniform MIL-88A(Fe) for enhanced visible light-driven photodegradation of RhB. *Applied Catalysis B: Environmental, 221*, 119–128. https://doi.org/10.1016/j.apcatb.2017.08.072

[14] Ding, S., Ren, X., Chen, R., & et al. (2023). Efficient degradation of phenol by 1T/2H-MoS2 /CuFe2O4 activated peroxymonosulfate and mechanism research. *Applied Surface Science, 612*, 155931. https://doi.org/10.1016/j.apsusc.2022.155931

[15] Li, F., Yuan, C., Niu, Y., & et al. (2024). Cobalt/iron bimetallic oxide coated with graphitized nitrogen-doped carbon (Fe2O3-CoO@NC) derived from cobalt/iron solid complex as peroxymonosulfate (PMS) activator for efficient bensulfuron-methyl degradation. *Environmental Research, 263*, 120249. https://doi.org/10.1016/j.envres.2024.120249

[16] Wang, D., Suo, M., Lai, S., & et al. (2023). Photoinduced acceleration of Fe3+/Fe2+ cycle in heterogeneous FeNi-MOFs to boost peroxodisulfate activation for organic pollutant degradation. *Applied Catalysis B: Environmental, 321*, 122054. https://doi.org/10.1016/j.apcatb.2022.122054

[17] Wang, B., Qian, K., Yang, W., & et al. (2023). ZnFe2O4/BiVO4 Z-scheme heterojunction for efficient visible-light photocatalytic degradation of ciprofloxacin. *Frontiers of Chemical Science and Engineering, 17*(11), 1728–1740. https://doi.org/10.1007/s11705-023-2322-z

[18] Zhang, Y., Guo, F., Di, J., & et al. (2024). Strain-induced surface interface dual polarization constructs PML-Cu/Bi12O17Br2 high-density active sites for CO2 photoreduction. *Nano-Micro Letters, 16*(1), 90. https://doi.org/10.1007/s40820-023-01276-6

[19] Zhang, J., Zhou, Y., Fang, Y., & et al. (2024). Chalcopyrite functionalized ceramic membrane for micropollutants removal and membrane fouling control via peroxymonosulfate activation: The synergy of nanoconfinement effect and interface interaction. *Journal of Colloid and Interface Science, 658*, 714–727. https://doi.org/10.1016/j.jcis.2023.12.093

[20] Jing, J., Pervez, M. N., Sun, P., & et al. (2021). Highly efficient removal of bisphenol A by a novel Co-doped LaFeO3 perovskite/PMS system in salinity water. *Science of The Total Environment, 801*, 149490. https://doi.org/10.1016/j.scitotenv.2021.149490

[21] Ni, T., Yang, Z., Zhang, H., & et al. (2022). Peroxymonosulfate activation by Co3O4/SnO2 for efficient degradation of ofloxacin under visible light. *Journal of Colloid and Interface Science, 615*, 650–662. https://doi.org/10.1016/j.jcis.2022.02.001

[22] Guo, T., Jiang, L., Wang, K., & et al. (2021). Efficient persulfate activation by hematite nanocrystals for degradation of organic pollutants under visible light irradiation: Facet-dependent catalytic performance and degradation mechanism. *Applied Catalysis B: Environmental, 286*, 119883. https://doi.org/10.1016/j.apcatb.2021.119883

[23] Qian, J., Zhang, Y., Chen, Z., & et al. (2023). Sulfur-decorated Fe/C composite synthesized from MIL-88A(Fe) for peroxymonosulfate activation towards tetracycline degradation: Multiple active sites and non-radical pathway dominated mechanism. *Journal of Environmental Management, 344*, 118440. https://doi.org/10.1016/j.jenvman.2023.118440

[24] Zhang, X., Zhang, Y., Tian, J., & et al. (2024). Generating 1O2 and CoIV=O through efficient peroxymonosulfate activation by ZnCo2O4 nanosheets for pollutant control. *Nano Research, 17*(9), 8025–8035. https://doi.org/10.1007/s12274-024-6689-2

[25] Tsitonaki, A., Petri, B., Crimi, M., & et al. (2010). In situ chemical oxidation of contaminated soil and groundwater using persulfate: A review. *Critical Reviews in Environmental Science and Technology, 40*(1), 55–91. https://doi.org/10.1080/10643380802209716

[26] Li, Y., Liu, L., Li, W., & et al. (2021). Simultaneously rapid degradation of phenylphosphonic acid and efficient adsorption of released phosphate in the system of peroxymonosulfate (PMS) and Co3O4-La2O2CO3/C derived from MOFs. *Journal of Environmental Chemical Engineering, 9*(6), 106332.

https://doi.org/10.1016/j.jece.2021.106332

[27] Zhao, Y., Wang, H., Li, X., & et al. (2021). Recovery of CuO/C catalyst from spent anode material in battery to activate peroxymonosulfate for refractory organic contaminants degradation. *Journal of Hazardous Materials, 420*, 126552. https://doi.org/10.1016/j.jhazmat.2021.126552

[28] Li, X., Wang, S., Xu, B., & et al. (2022). MOF etching-induced Co-doped hollow carbon nitride catalyst for efficient removal of antibiotic contaminants by enhanced perxymonosulfate activation. *Chemical Engineering Journal, 441*, 136074. https://doi.org/10.1016/j.cej.2022.136074

[29] Liu, J., Zhou, J., Ding, Z., & et al. (2017). Ultrasound irritation enhanced heterogeneous activation of peroxymonosulfate with Fe3O4 for degradation of azo dye. *Ultrasonics Sonochemistry, 34*, 953–959. https://doi.org/10.1016/j.ultsonch.2016.07.018

[30] Golshan, M., Kakavandi, B., Ahmadi, M., & et al. (2018). Photocatalytic activation of peroxymonosulfate by TiO2 anchored on copper ferrite (TiO2@CuFe2O4) into 2,4-D degradation: Process feasibility, mechanism and pathway. *Journal of Hazardous Materials, 359*, 325–337. https://doi.org/10.1016/j.jhazmat.2018.07.033

[31] Hu, L., Zhang, G., Liu, M., & et al. (2018). Enhanced degradation of bisphenol A (BPA) by peroxymonosulfate with Co3O4-Bi2O3 catalyst activation: Effects of pH, inorganic anions, and water matrix. *Chemical Engineering Journal, 338*, 300–310. https://doi.org/10.1016/j.cej.2018.01.013

[32] Liu, Y., Guo, H., Zhang, Y., & et al. (2019). Fe@C carbonized resin for peroxymonosulfate activation and bisphenol S degradation. *Environmental Pollution, 252*, 1042–1050. https://doi.org/10.1016/j.envpol.2019.06.018

[33] Li, N., Wang, Y., Cheng, X., & et al. (2022). Influences and mechanisms of phosphate ions onto persulfate activation and organic degradation in water treatment: A review. *Water Research, 222*, 118896. https://doi.org/10.1016/j.watres.2022.118896

[34] Fu, H., Ma, S., Zhao, P., & et al. (2019). Activation of peroxymonosulfate by graphitized hierarchical porous biochar and MnFe2O4 magnetic nanoarchitecture for organic pollutants degradation: Structure dependence and mechanism. *Chemical Engineering Journal, 360*, 157–170. https://doi.org/10.1016/j.cej.2018.11.197

[35] Zhao, Y., Song, M., Cao, Q., & et al. (2020). The superoxide radicals' production via persulfate activated with CuFe2O4@Biochar composites to promote the redox pairs cycling for efficient degradation of o-nitrochlorobenzene in soil. *Journal of Hazardous Materials, 400*, 122887. https://doi.org/10.1016/j.jhazmat.2020.122887

[36] Sun, X., Xu, D., Dai, P., & et al. (2020). Efficient degradation of methyl orange in water via both radical and non-radical pathways using Fe-Co bimetal-doped MCM-41 as peroxymonosulfate activator. *Chemical Engineering Journal, 402*, 125881. https://doi.org/10.1016/j.cej.2020.125881

[37] Guan, Y.-H., Ma, J., Ren, Y.-M., & et al. (2013). Efficient degradation of atrazine by magnetic porous copper ferrite catalyzed peroxymonosulfate oxidation via the formation of hydroxyl and sulfate radicals. *Water Research, 47*(14), 5431–5438. https://doi.org/10.1016/j.watres.2013.06.023

[38] Ding, Y., Zhu, L., Wang, N., & et al. (2013). Sulfate radicals induced degradation of tetrabromobisphenol A with nanoscaled magnetic CuFe2O4 as a heterogeneous catalyst of peroxymonosulfate. *Applied Catalysis B: Environmental, 129*, 153–162. https://doi.org/10.1016/j.apcatb.2012.09.015

[39] Wang, N., Liu, Y., Wu, C., & et al. (2022). SnO2 shells-induced rich Co2+ sites and oxygen vacancies in FexCo3-xO4 nanocubes: Enhanced peroxymonosulfate activation performance for water remediation. *Chemical Engineering Journal, 439*, 135682. https://doi.org/10.1016/j.cej.2022.135682